Journal of Materials Research and Technology 39 (2025) 6906–6914

Contents lists available at ScienceDirect

Journal of Materials Research and Technology

journal homepage: www.elsevier.com/locate/jmrt

Mechanical property evolution of ZE10A alloy subjected to thermomechanical treatments between 250 and 300 °C

Eduardo Luis Schneider [a,*], Charles Amaral de Jesus Cordeiro [a], Rodrigo Nazarof Saran [a], Jakson Manfredini Vassoler [b], Diego Tolotti de Almeida [c], Claudia Trindade Oliveira [d], Lisete Cristine Scienza [a], Fabrício Luiz Faita [e]

[a] Programa de Pós-Graduação em Engenharia de Minas, Metalúrgica e de Materiais (PPGE3M), Universidade Federal do Rio Grande do Sul (UFRGS), 91509-900, Porto Alegre, RS, Brazil
[b] Programa de Pós-Graduação em Engenharia Mecânica (PROMEC), Universidade Federal do Rio Grande do Sul (UFRGS), 90040-001, Porto Alegre, RS, Brazil
[c] Bruning Tecnometal Ltda., 98280-000, Panambi, RS, Brazil
[d] Programa de Pós-Graduação Profissional em Tecnologia de Materiais e Processos Industriais, Universidade Feevale, 93352-000, Novo Hamburgo, RS, Brazil
[e] Programa de Pós-Graduação em Física - PPGFis and Programa de Pós-Graduação em Ciências do Materiais - PPGCIMAT, Universidade Federal do Rio Grande do Sul (UFRGS), 91501-970, Porto Alegre, RS, Brazil

ARTICLE INFO

Keywords:
Magnesium alloy
Rare earth
Neodymium
Thermomechanical treatments
Microstructure
Mechanical properties
ZE10A

ABSTRACT

Magnesium alloys containing rare earth elements have been developed to improve ductility and reduce anisotropy. The ZE10A alloy (Elektron® 717) has demonstrated good performance in hot stamping applications. However, the formability of sheets made from this alloy at temperatures below 350 °C remains insufficiently studied. This work aims to investigate the relationship between thermomechanical treatments in the temperature range of 250–300 °C and the resulting mechanical properties and microstructural evolution of the ZE10A alloy. Uniaxial tensile tests were carried out at 250 °C, 275 °C, and 300 °C at a strain rate of 0.26 s^{-1} to evaluate the yield strength, ultimate tensile strength, and elongation. The microstructure of the specimens was analyzed by optical microscopy, including average grain size measurements, and by complementary X-ray diffraction (XRD). The results showed that, as the temperature increased from 250 °C to 300 °C, the yield strength decreased by 11.7 %, the ultimate tensile strength by 15.7 %, and the elongation by 2.7 %. Microstructural analysis revealed a transition from slightly elongated grains at 250 °C to partially equiaxed grains at 300 °C, consistent with incipient dynamic recrystallization (DRX). The average grain size decreased from 14.19 μm at 250 °C to 12.61 μm at 300 °C, suggesting the onset of DRX, although its extent may be limited by the presence of neodymium. XRD indicated that ZE10A behaves as a nearly single-phase material within this temperature window (all detectable peaks from α-Mg), with no clear evidence of Mg–Nd precipitates; a slight attenuation of {10–12} twin-related reflections with temperature suggests twin relaxation and recovery/incipient DRX. These findings clarify deformation accommodation in ZE10A at 250–300 °C and support the feasibility of processing in this low-temperature window with a balanced trade-off between strength retention and formability.

1. Introduction

The most remarkable characteristic of magnesium is its density of 1.74 g/cm^3, the lowest among all structural metals, which makes its alloys highly preferred due to their weight reduction capability [1–6]. In addition to lightness, impact and vibration resistance are also factors that make its use advantageous [7]. Most magnesium parts used in automotive applications are produced by high-pressure die casting. However, cast magnesium parts often exhibit low fatigue strength and ductility [8]. In contrast, wrought magnesium alloys typically present superior mechanical properties, such as tensile and fatigue strength.

Hot tensile tests have been widely used by several authors to evaluate the hot formability of magnesium alloys [9], and some studies have linked the increase in grain size to a decrease in resistance to plastic deformation [10–12]. Moreover, various studies have demonstrated that magnesium alloys are highly suitable for sheet forming processes due to

* Corresponding author.
E-mail address: prof.eduardo@ufrgs.br (E.L. Schneider).

https://doi.org/10.1016/j.jmrt.2025.10.266
Received 8 August 2025; Received in revised form 7 October 2025; Accepted 7 October 2025
Available online 8 November 2025
2238-7854/© 2025 The Authors. Published by Elsevier B.V. This is an open access article under the CC BY-NC license (http://creativecommons.org/licenses/by-nc/4.0/).

their high strain-hardening coefficient (n) and high true strain ratio (r) [13–15]. Nevertheless, the mechanical forming of magnesium alloys is still limited due to their poor formability at room temperature [16,17]. This low formability is attributed to their hexagonal close-packed (HCP) structure and the corresponding mechanical anisotropy [18,19].

In recent years, there has been renewed interest from the aerospace, military, and medical industries in the development of new magnesium alloys [20,21]. One of the most promising ways to improve the mechanical properties and creep resistance of magnesium alloys is through the addition of rare earth elements [22]. Rare earth (RE) containing Mg alloys have been developed to enhance ductility and strength, while reducing anisotropy and tension–compression asymmetry compared to conventional Mg alloys [22]. Rare earth elements such as cerium (Ce), gadolinium (Gd), and neodymium (Nd) are among the most commonly used in commercial magnesium alloys and have shown favorable effects on microstructure and improved mechanical properties [23].

ZE10A, also known as ZEK100, is a magnesium alloy containing up to 0.22 % Nd, commercially available as ZE10A. This alloy stands out due to its hot formability and corrosion resistance [24,25]. Table 1 lists the minimum mechanical properties of the ZE10A alloy for two sheet thickness ranges.

A study on ZE10A (ZEK100) tensile tests at room temperature in the O condition (annealed at 450 °C for 1 h and furnace-cooled to room temperature) reported a yield strength of 130 MPa, ultimate tensile strength of 250 MPa, and elongation of 17 %, showing slightly higher values than those provided in the manufacturer's datasheet [24]. Another experimental investigation using uniaxial tensile tests at elevated temperatures (350 °C and 450 °C) and strain rates of 0.1–5 s^{-1} evaluated the mechanical properties and related them to dynamic recrystallization and grain size variations [26]. The yield strength decreased from approximately 135 MPa at 350 °C to 95 MPa at 450 °C, while the ultimate tensile strength decreased from around 180 MPa–140 MPa. The ductility of the samples increased with both temperature and strain rate. Higher ductility at higher strain rates was mainly attributed to finer grain sizes and slightly weakened textures, allowing more uniform deformation. Furthermore, the asymmetric deformation response and anisotropy in magnesium sheet alloys, particularly in ZEK100 systems closely related to ZE10A, have been previously modeled and characterized in detail [27].

In magnesium alloys, extension (tensile) twinning ({10–12}⟨10–11⟩) is a dominant deformation mode at room temperature and low to intermediate strain rates, especially when the c-axis is under tension. However, its activity decreases progressively with increasing temperature, since non-basal slip systems become easier to activate and partially replace twinning as an accommodation mechanism [28,29]. This effect is further influenced by the addition of rare-earth elements, such as Nd in ZE10A, which not only modify the critical resolved shear stresses of slip systems but also reduce the overall twin fraction through solute drag and texture randomization [30–32]. As a result, the balance between twinning, slip, and dynamic recovery/recrystallization strongly depends on the testing temperature and alloy chemistry.

Several advanced characterization techniques have been employed to identify and quantify the active deformation mechanisms in Mg alloys. X-ray diffraction (XRD) has proven effective for detecting twinning signatures through peak splitting and intensity changes, while SEM and TEM provide direct insights into twin morphology, dislocation structures, and interactions with secondary phases [33]. Although EBSD offers the most complete picture of twin variant selection and recrystallized fractions, XRD combined with electron microscopy remains a reliable approach to correlate twinning activity with mechanical response under warm deformation conditions. These aspects are particularly relevant for ZE10A, where limited DRX and the suppression of twinning by Nd can significantly affect the mechanical performance [34].

Despite significant advances, these studies did not address the mechanical behavior and microstructure of this magnesium alloy at lower temperature ranges, which could support the development of cost-effective, energy-saving, and efficient forming techniques for producing parts and components. Warm forming of this alloy remains challenging for both industry and academia. A clear understanding of its potential and limitations is crucial to achieving the required technological maturity.

Thus, the aim of this work was to investigate the warm mechanical behavior of the Mg ZE10A alloy through tensile tests at 250, 275, and 300 °C with a strain rate of 0.26 s^{-1} and to evaluate the influence of these thermomechanical treatments on the average grain sizes. The results provide insights into the mechanical behavior of ZE10A within a previously unexplored temperature range and contribute to the feasibility of its application in sheet-forming processes with lower energy consumption for components such as curved sheets and profiles.

2. Materials and methods

The material used in this study was a 800 × 1000 mm × 1.4 mm sheet manufactured by Luxfer Magnesium, alloy ASTM B90 ZE10A (Elektron® 717). Its chemical composition is listed in Table 2. This alloy is considered quasi-monophasic due to the presence of a small fraction of Zn–Zr/Nd-rich intermetallic second phase [23].

Rectangular tensile specimens were cut by laser with their longitudinal axis parallel (0°) to the rolling direction, following standard dimensions according to ASTM A370-23 [35] and ASTM E8/E8M-16ae1 [36] for subsize specimens. The specimen geometry is shown in Fig. 1, and the dimensions are listed in Table 3.

Based on ASTM B557M − 15 [37], tensile tests were conducted at 250, 275, and 300 °C using a crosshead speed of 500 mm/min. Considering the reduced gauge length of the specimen (32 mm), this corresponds to an average initial strain rate of approximately 0.26 s^{-1}, as estimated by Eq. (1)

$$\dot{\varepsilon} = v/Lo \quad (1)$$

where $\dot{\varepsilon}$ is the strain rate, v is the crosshead speed, and L_0 is the length of the reduced parallel section. It should be noted that the applied crosshead speed of 500 mm/min corresponds to the maximum speed available in the testing machine. This choice was intentional, as it provides an average strain rate of 0.26 s^{-1}, which is consistent with Eq. (1) and closer to the cycle times typically encountered in industrial warm-forming and hot-stamping presses. The overall experimental workflow is illustrated in Fig. 2, which presents a schematic diagram of the tensile test setup, the specimen geometry and orientation (tensile axis parallel to the rolling direction), and the regions selected for post-fracture metallographic analysis.

Table 1
Minimum mechanical properties of ZE10A alloy.

Thickness (mm)	Yield strength (MPa)	Ultimate tensile strength (MPa)	Elongation (%)
1–1.52	124	207	15
1.53–6.35	103	207	15

Source: Adapted from Luxfer (2018) [24] and ASTM B90/B90M − 21 (2023) [25].

Table 2
Chemical composition of ZE10A alloy.

Zn (wt.%)	Nd (wt.%)	Zr (wt.%)	Mg
1.0–1.5	0.12–0.22	≥0.2	Balance

Source: Adapted from Luxfer (2018) [24] and ASTM B90/B90M − 21 (2023) [25].

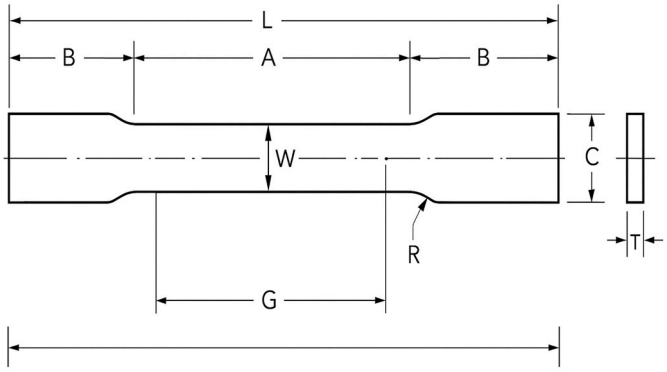


Fig. 1. Geometry of subsize tensile specimens used in this study.
Source: Adapted from ASTM E8M [36].

Table 3
Dimensions of subsize tensile specimens.

Parameter	Dimension (mm)
G – Gauge length	25.0 ± 0.1
W – Width	6.0 ± 0.1
T – Thickness	1.4
R – Radius of fillet	6
L – Overall length	100
A – Reduced section	32
B – Grip section length	30
C – Grip section width	10

Source: Adapted from ASTM E8M [36].

2.1. Characterization by optical microscopy (OM)

Samples were extracted from the tensile specimens and prepared for metallography and chemical analysis. Specimens were sectioned in two regions — the head and the gauge region (where plastic deformation occurs).

Samples were prepared according to ASTM E3-11 (2017) [39], embedded in methyl methacrylate (PMMA-EA) resin with catalyst. After curing, the samples were ground using SiC papers of #220, #320, #400, #600, and #1200 grit, and then polished on a rotating disk with 0.5 μm alumina. Chemical etching was performed with Nital solution to reveal grain boundaries [40].

OM was performed on an inverted optical microscope at 500 × magnification. Grain size determination was carried out using the linear intercept method in accordance with ASTM E112-13 [38]. Average intercept lengths were obtained by overlaying 4 horizontals and 5 vertical lines on the micrographs using ImageJ software, counting grain boundary intersections. For each temperature, the average linear intercept was calculated and converted into the ASTM grain size number (G).

2.2. Characterization by XRD

To complement OM observations, X-ray diffraction (XRD) analyses were carried out using a Rigaku Ultima IV diffractometer equipped with Cu Kα radiation (λ = 1.5406 Å) operating in θ–2θ geometry. The ZE10A alloy specimens were analyzed without sample rotation (no spinner), ensuring consistent spot positions between temperature conditions. Wide scans from 20° to 90° 2θ were performed to identify global phase constituents. Focused high-resolution scans targeted specific angular windows to investigate characteristic reflections: (i) 30–36° for the basal (0002) reflection of α-Mg and adjacent peaks; (ii) 60–65° corresponding to the {10–12} twinning region; and (iii) 28–31°, where possible Mg–RE or Mg–Zn precipitate reflections could appear. Step scans (0.01°, 8 s/step) were applied to the 28–31° range to enhance signal-to-noise ratios for weak peaks. Continuous scans (0.01°, ≈4 s/°) were executed for the 30–36° and 60–65° ranges, each repeated five times and summed to increase statistical precision while maintaining identical conditions for all temperatures. The X-ray tube was operated at 40 kV and 25 mA using Cu Kα radiation (λ = 1.5418 Å), and these parameters were kept constant for all scans. The complete measurement configuration is summarized in Table 4.

To reduce repositioning bias and total acquisition time, the 28–36° (2θ) region for the 275 °C specimen was collected in a single continuous scan, replacing the separate 31–36° window used at 250 °C and 300 °C. This choice also kept exactly the same alignment between the precipitate window (28–31°) and the basal (0002) window (31–36°) and increased counting statistics for the (0002) peak in one pass. The angular step and the effective dwell per step (0.02°; ~0.20 s after summing 5 passes) matched those used for the 31–36° acquisitions at the other temperatures, ensuring full comparability of 2θ and FWHM metrics across conditions. The 28–31° step scan was still collected at 275 °C to verify the absence of precipitate peaks.

No pole figures were acquired; θ–2θ scans were run at fixed

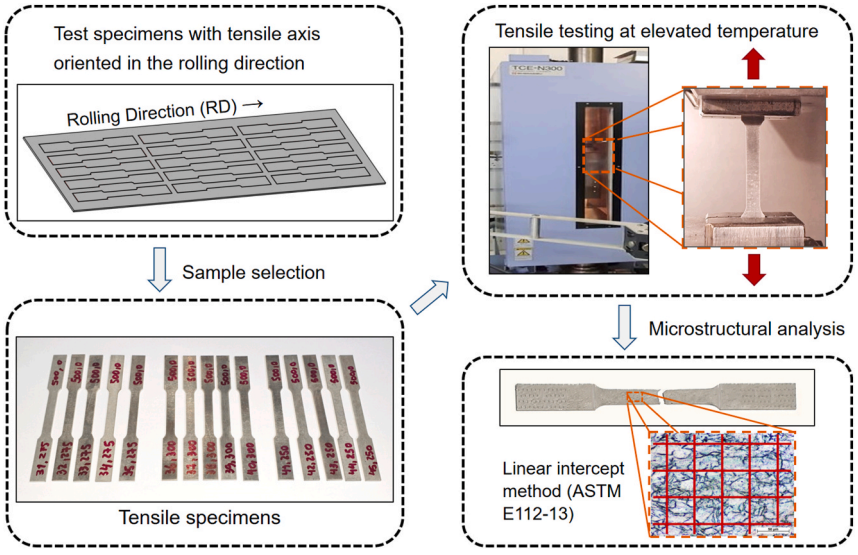


Fig. 2. Schematic representation of the experimental workflow, including specimen orientation along the rolling direction (RD), tensile testing setup at elevated temperature, and microstructural analysis using the linear intercept method (ASTM E112-13 [38]).

Table 4
XRD scan parameters for ZE10A alloy samples measured with Rigaku Ultima IV.

Temperature (°C)	2θ range (°)	Step size (°)	Mode	Time per step/scan	Repetitions	Notes
250	20–90	0.020	Wide scan	–	1	Global phase reference
250	28–31	0.010	Step scan	8 s/step	1	High SNR for weak Mg–RE peaks
250	31–36	0.010	Continuous	≈4 s/° (5 × summed)	5	Basal (0002) and nearby peaks
250	60–65	0.010	Continuous	≈4 s/° (5 × summed)	5	Twinning {10–12} region
275	20–90	0.020	Wide scan	–	1	Global phase reference
275	28–36	0.010	Continuous[a]	≈4 s/° (5 × summed)	5	Combined window (0002 + Mg–RE)
275	28–31	0.010	Step scan	8 s/step	1	High SNR, precipitate region
275	60–65	0.010	Continuous	≈4 s/° (5 × summed)	5	Twinning {10–12} region
300	20–90	0.020	Wide scan	–	1	Global phase reference
300	28–31	0.010	Step scan	8 s/step	1	High SNR for weak Mg–RE peaks
300	31–36	0.010	Continuous	≈4 s/° (5 × summed)	5	Basal (0002) and nearby peaks
300	60–65	0.010	Continuous	≈4 s/° (5 × summed)	5	Twinning {10–12} region

Notes: SNR – signal-to-noise ratio; RE – rare earth. Time values correspond to the acquisition setup defined by the operator; for continuous mode, total effective dwell per step is approximately 0.20 s after summing 5 scans.

[a] At 275 °C, a single 28–36° continuous scan was used (replacing a separate 31–36° window); (0002) peak parameters were extracted from this dataset. A 28–31° step scan was also acquired to check for Mg–Nd precipitate peaks.

orientation and without spinning. All specimens were mounted with identical in-plane orientation and measured under identical settings; to minimize bias from preferred orientation, we interpret intensities qualitatively within the same series and emphasize peak positions/FWHM over absolute counts. Texture quantification is left for future work.

Peak profiles were fitted with a pseudo-Voigt function to extract the FWHM (in degrees 2θ). Instrumental broadening was determined from a strain-free silicon standard acquired under identical conditions, and the sample broadening was computed as $\beta^* = \sqrt{(\beta_meas^2 - \beta_inst^2)}$ (β in radians for any auxiliary calculations). Given the limited number of strong reflections under the present sheet texture, we report instrument-corrected FWHM trends for (0002) and (10$\bar{1}$0) in the main text (Table 7).

3. Results

The results of the tensile tests carried out on the ZE10A alloy at 250 °C, 275 °C, and 300 °C with a strain rate of 0.26 s^{-1} are summarized in Table 5, which lists the mean values and standard deviations of the mechanical properties, including yield strength (YS), ultimate tensile strength (UTS), and true strain (% ε_t). Fig. 3 shows the true stress–true strain curves, with one representative curve plotted for each temperature, selected based on their behavior being closest to the mean parameters. Fig. 4 presents the mean and standard deviation (SD) values of YS, UTS, true strain at UTS (ε_t,UTS), and true strain at fracture (ε_t,f) for the three temperatures.

3.1. Microstructural characterization

The microstructures of the samples after tensile tests at 250 °C, 275 °C, and 300 °C are shown in Fig. 5. Table 6 lists the results of the grain size evaluation obtained by the linear intercept method for these temperatures. Fig. 6 compares the average grain size of ZE10A across the same temperature range. Grain size values were obtained from at least three micrographs per temperature condition, each evaluated by the linear intercept method (ASTM E112) using multiple measurement lines, and are reported as mean ± SD.

As observed in Fig. 5, the microstructure of the alloy at 250 °C shows slightly elongated grains, typical of deformation via dislocation motion and deformation twinning, with little evidence of dynamic recrystallization (DRX). At 275 °C, the microstructure is characterized by slightly larger grains, fewer twins, and the initial formation of localized equiaxed grains along specific grain boundary regions. At 300 °C, a larger fraction of equiaxed grains is observed, distributed along the initial grain boundaries, along with fewer twins — all features indicative of a slightly higher DRX fraction. Grain refinement remains limited since the thermal energy is insufficient to promote significant nucleation of new grains, and Nd also contributes to restraining grain growth.

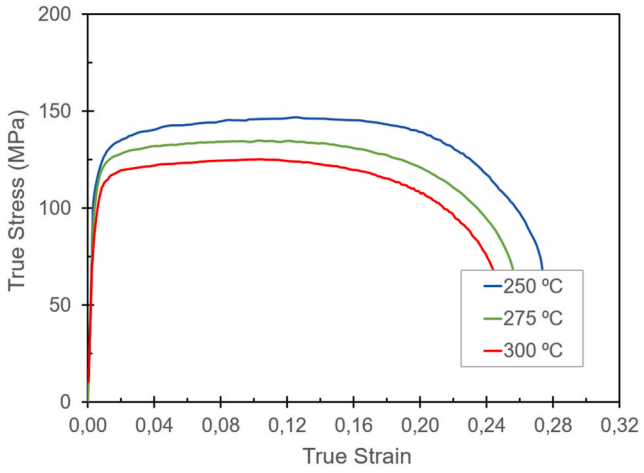


Fig. 3. True stress–strain curves of ZE10A alloy tested at 250, 275, and 300 °C with strain rate of 0.26 s^{-1}.

3.2. Characterization by XRD

The X-ray diffraction (XRD) patterns of the ZE10A alloy obtained at 250 °C, 275 °C, and 300 °C are shown in Figs. 7–9. These analyses were conducted to complement the optical microscopy observations and identify possible phase evolution or residual stress relaxation with

Table 5
Tensile results of ZE10A at 250 °C, 275 °C, and 300 °C: yield strength (YS), ultimate tensile strength (UTS), true strain at UTS (ε_t,UTS), and at fracture (ε_t,f). Values are presented as mean ± SD.

Temperature (°C)	YS (MPa)	UTS (MPa)	ε_t,UTS	ε_t,f
250	90.06 ± 0.69	150.11 ± 6.17	0.133 ± 0.018	0.284 ± 0.039
275	86.18 ± 4.05	135.69 ± 5.44	0.119 ± 0.008	0.259 ± 0.021
300	79.50 ± 5.50	126.49 ± 2.13	0.105 ± 0.006	0.251 ± 0.007

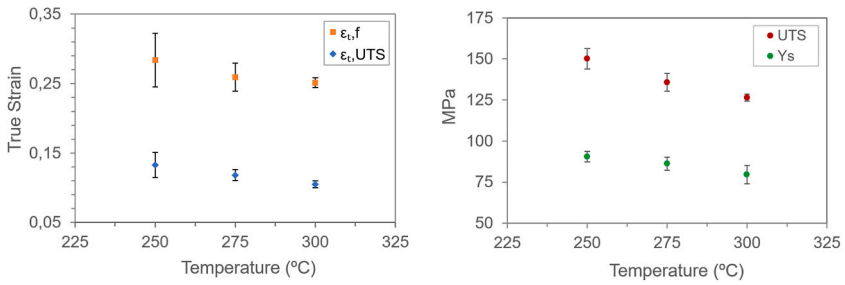


Fig. 4. (A) Yield strength (YS) and ultimate tensile strength (UTS). (B) True strain at UTS (ε_t,UTS) and at fracture (ε_t,f) for 250 °C, 275 °C, and 300 °C.

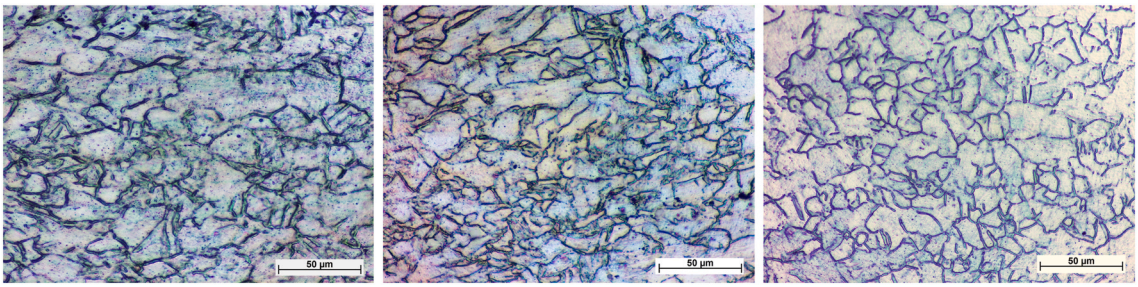


Fig. 5. Optical micrographs of ZE10A alloy after tensile testing at: (a) 250 °C, (b) 275 °C, and (c) 300 °C. Etching with Nital. Grain morphology shows partial recrystallization with increasing temperature.

Table 6
Average linear intercept (mean ± SD) and corresponding ASTM grain size numbers determined by the linear intercept method for each temperature. Standard deviations are reported only for the linear intercept values, since ASTM grain size numbers were derived directly from these averages.

Temperature (°C)	Average intercept (µm)	ASTM G
250	14.19 ± 1.17	8.98
275	12.87 ± 0.99	9.27
300	12.61 ± 1.04	9.32

Note: Values reported as mean ± SD (ASTM E112) from multiple fields across replicate specimens for each temperature.

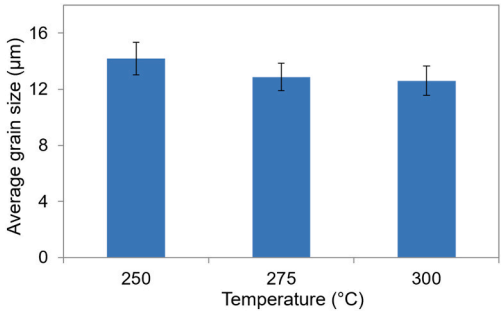


Fig. 6. Average grain size variation of ZE10A alloy with increasing temperature, showing slight refinement from 250 °C to 300 °C. Measured using the linear intercept method (ASTM E112-13 [38]). Error bars represent ±1 SD across multiple fields/replicates; the scatter reflects the intrinsic heterogeneity of partially recrystallized microstructures.

Table 7
FWHM of selected reflections (measured, uncorrected; degrees 2θ).

Reflection	250 °C FWHM* (°2θ)	275 °C FWHM* (°2θ)	300 °C FWHM* (°2θ)
(0002)	0.164	0.179	0.164
(10–10)	0.159	0.179	0.167

Notes: Values are measured FWHM from pseudo-Voigt-like local fits to raw profiles, without instrumental correction. If a silicon standard measured under identical conditions is provided, instrumental broadening can be removed ($\beta^* = \sqrt{(\beta_meas^2 - \beta_inst^2)}$).

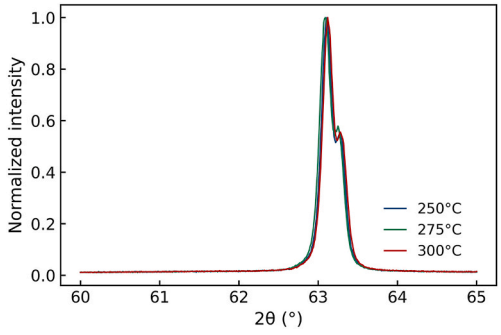


Fig. 7. XRD patterns of ZE10A alloy measured from 20° to 90° (2θ) after thermomechanical treatments at 250 °C, 275 °C, and 300 °C. All peaks correspond to the α-Mg phase ($P6_3/mmc$), with no additional reflections attributable to Mg–Nd compounds within the detection limits, indicating stable lattice parameters across the studied temperature range.

temperature.

Fig. 7 presents the diffractograms collected in the 20–90° 2θ range. All diffraction peaks correspond to the hexagonal α-Mg phase (space group $P6_3/mmc$), with no additional reflections attributable to intermetallic compounds. The XRD results indicate that the ZE10A alloy behaves as a nearly single-phase material within the investigated temperature range. All detectable peaks correspond to the α-Mg phase, and no clear evidence of secondary Mg–Nd compounds (e.g., $Mg_{12}Nd$ or $Mg_{41}Nd_5$) was observed. This is consistent with the low solute content and slow precipitation kinetics expected for Nd-containing ZE-series alloys below 350 °C. Peak positions remain constant, indicating no measurable lattice expansion within the resolution of the diffractometer.

In the detailed region of 28–36° 2θ (Fig. 8), the basal (0002) reflection remains dominant at all temperatures, with FWHM values

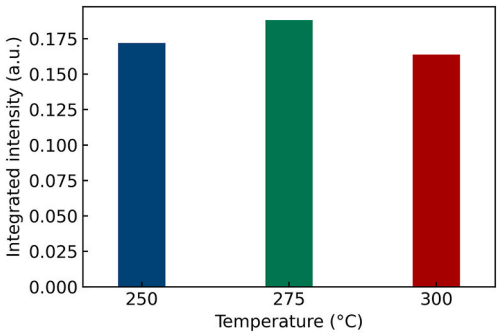


Fig. 8. High-resolution XRD profiles of ZE10A alloy in the 28–36° (2θ) range, showing the basal (0002) reflection of α-Mg and possible weak features near 30° (2θ). No significant angular shifts or FWHM changes are observed, confirming minimal residual stress and absence of Mg–Nd precipitate peaks within the detection limits. Measured (uncorrected) FWHM values for (0002) and (10 $\bar{1}$ 0) are given in Table 7.

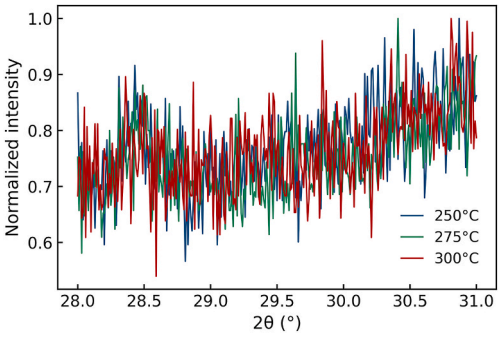


Fig. 9. Comparison of XRD intensity profiles in the 60–65° (2θ) range, corresponding to {10–12} twin-related reflections (tensile twins) for specimens tested at 250 °C, 275 °C, and 300 °C. A slight reduction in twin-related peak intensity with increasing temperature indicates progressive twin relaxation and early dynamic recovery.

measured (uncorrected) and summarized in Table 7. This suggests the absence of significant residual stresses or plastic strain accumulation after testing. Weak humps near 30° 2θ may correspond to background noise rather than identifiable Mg–RE phases such as $Mg_{12}Nd$ or $Mg_{41}Nd_5$, whose expected intensity would be below the detection limit for the current setup. These results confirm that the ZE10A alloy exhibits structural stability during the thermomechanical treatments applied at 250–300 °C.

To substantiate the assessment of residual strain and recovery, the measured (uncorrected) FWHM of the (0002) and (10 $\bar{1}$0) reflections was evaluated at all temperatures (Table 7). Within the experimental uncertainty, no systematic FWHM increase is observed across 250–300 °C, which is consistent with low residual microstrain and limited changes in defect density within this window.

Fig. 9 compares the intensity profiles in the 60–65° 2θ range, corresponding to the {10–12} twinning-related reflections consistent with {10–12} tensile twins. Although the absolute intensity of this region is low, a slight decrease in relative intensity is noted as temperature increases, suggesting progressive stress relaxation and reduced twin fraction. This trend aligns with the optical observations (Fig. 5) that showed fewer twins and more equiaxed grains at 300 °C, consistent with the onset of dynamic recovery and incipient DRX. The combination of these results indicates that in the 250–300 °C interval, the ZE10A alloy mainly undergoes strain accommodation through dislocation slip and partial twinning suppression, without the formation of detectable secondary phases.

Additional high-resolution spectra and comparative 2θ windows are provided in the Supplementary Fig. S1–S2, which illustrate in greater detail the {10–12} twinning region and the basal (0002) reflection discussed in this section.

4. Discussion

4.1. Mechanical behavior

Analyzing the data in Table 5 and Fig. 4A, the yield strength (YS) decreased by approximately 11.7 % when the temperature increased from 250 °C to 300 °C. This reduction was about 4.3 % between 250 °C and 275 °C and 7.7 % between 275 °C and 300 °C, indicating progressive loss of resistance to the onset of plastic deformation as temperature rises. Compared to previous tensile tests at 350 °C and 450 °C on ZE10A [26], where YS dropped by 29.6 %, the smaller reduction in this study can be attributed to the lower temperature range and the less intense activation of deformation mechanisms.

Similarly, the ultimate tensile strength (UTS) decreased by approximately 15.7 % from 250 °C to 300 °C, with sharper drops of 9.6 % between 250 °C and 275 °C and 6.8 % between 275 °C and 300 °C. For the 350–450 °C range [26], UTS fell by 22.2 %, reflecting stronger thermal softening due to enhanced dynamic recrystallization (DRX) and increased dislocation mobility at higher temperatures.

Regarding true strain, the strain at UTS (ε_t,UTS) dropped from 0.133 (250 °C) to 0.105 (300 °C), and the fracture strain (ε_t,f) decreased from 0.284 to 0.251. This suggests the plastic deformation capacity reduces with temperature increase, likely due to thermal softening and reduced strain-hardening capability. The difference between strain at UTS and fracture narrowed slightly (0.15 at 250 °C to 0.14 at 300 °C), indicating earlier onset of plastic instability and less pronounced necking. This ductility loss (~12 %) is similar to that observed in the AZ91 alloy (~13.6 %) [41]. A comprehensive description of the role of {10–12} tensile twinning and its temperature-dependent attenuation in wrought Mg alloys is provided in Shah et al. [42].

The reduction in ductility can be explained by temperature-dependent deformation mechanisms: up to 250 °C, non-basal slip systems activate, temporarily enhancing ductility [35]; however, by 300 °C, increased dislocation mobility, recovery, and early DRX onset reduce strain hardening, leading to premature plastic instability and intensified microvoid coalescence. In contrast, at 350–450 °C, larger DRX volume promotes a significant increase in strain to failure [26,43]. Although Nd addition limits DRX in pure Mg, higher temperatures favor recrystallized fraction growth and microstructure refinement [44], improving uniform plastic deformation.

4.2. Grain size and DRX behavior

Fig. 6 shows that the average grain size decreased slightly from 14.19 μm at 250 °C to 12.61 μm at 300 °C, representing an 11.1 % reduction. Grain size measurements were evaluated separately in the horizontal and vertical directions. The ratio between horizontal and vertical intercepts decreased with increasing temperature (1.30 at 250 °C, 1.28 at 275 °C, and 1.17 at 300 °C), indicating a tendency toward more equiaxed grains. This behavior is consistent with the occurrence of incipient DRX. Although the mean grain sizes at 275 °C (12.87 ± 0.99 μm) and 300 °C (12.61 ± 1.04 μm) are close and the standard deviations overlap, the data show a modest downward shift in the average grain size—from 14.19 μm at 250 °C to 12.61 μm at 300 °C—consistent with the emergence of more equiaxed grains and the limited DRX expected in this temperature window. The limited grain refinement observed can be partly explained by the dominance of softening mechanisms over Hall–Petch strengthening Eq. (2).

$$\sigma_y = \sigma_0 + k \cdot d^{-1}/^2 \quad (2)$$

According to the Hall–Petch relationship, this grain refinement

would typically increase yield strength. However, the observed decrease in YS indicates that thermally activated recovery and DRX mechanisms dominate over grain boundary strengthening in this temperature range. As summarized in Table 6, the average linear intercept decreases slightly from 14.19 μm (250 °C) to 12.61 μm (300 °C), consistent with limited DRX within this window.

Microstructural analysis (Fig. 5) reveals a transition from elongated, deformed grains with many twins at 250 °C to the formation of finer, equiaxed grains at 300 °C, consistent with incipient DRX. Compared to the significant DRX fraction (~40 %) reported in AZ31 at 300 °C [45,44], ZE10A shows limited DRX due to Nd's solute segregation, which inhibits grain boundary migration and grain growth [46]. Robson (2013) [47] also confirms that rare earth elements significantly delay DRX even under favorable conditions.

The grain sizes observed here are larger than those produced by severe plastic deformation methods such as ECAP [19] or controlled extrusion [48], but similar to those reported for ZE10A under conventional hot deformation [26]. For instance, previous studies at 350 °C and 450 °C [26] showed grain size reduced from 17.6 μm to ~12.5 μm due to DRX, followed by slight coarsening (~13.5 μm) at 450 °C. The smaller reduction in grain size in the current temperature range confirms DRX remains incipient.

Furthermore, the difference in strain rate explains variations in grain size: higher strain rates (e.g., 1 s^{-1}) promote more nucleation of new grains through twinning and DRX, leading to finer grains, while the lower strain rate used here (0.26 s^{-1}) favors grain growth. It is important to note that the recrystallized fraction was not quantified in this study due to the absence of electron backscatter diffraction (EBSD) analysis. The identification of DRX onset was based solely on morphological features observed in the optical micrographs, such as the emergence of finer equiaxed grains.

The literature reports that DRX fraction and grain growth kinetics follow sigmoidal or parabolic trends influenced by time, temperature, and alloy chemistry [45]. For example, ZK60, with Zr as a grain refiner, often shows smaller DRX fractions than AZ31 under similar conditions due to precipitate pinning [44], following the classical correlation between plastic deformation and dynamic recrystallization proposed by Galiyev et al. [46]. ZE10A, containing Nd, exhibits even stronger DRX suppression [47]. This trend confirms that rare-earth elements significantly delay DRX even under favorable thermomechanical conditions, as reported by Hantzsche et al. [49] and Robson (2013) [47]. Furthermore, the gradual decrease in twin density and the emergence of equiaxed grains at 300 °C (Fig. 5) suggest that recovery and incipient DRX act simultaneously, stabilizing the microstructure before full recrystallization occurs. A similar temperature-dependent transition between twinning and DRX-dominated deformation has been described for Mg–RE alloys by Hadorn et al. [50], indicating that solute drag from rare-earth elements can retard boundary mobility and delay complete recrystallization.

Although the tensile behavior and microstructure were extensively characterized, fracture surface analysis was not included in this study. Future work should incorporate scanning electron microscopy (SEM) observations to investigate fracture mechanisms and validate the ductile–brittle transition with temperature.

Even though only limited grain refinement and DRX onset were observed in the 250–300 °C range for ZE10A, processing at these lower warm-forming temperatures may offer industrial advantages in terms of energy efficiency. Gao et al. [51] reported that optimizing the hot stamping of magnesium alloys — particularly by reducing forming temperature and controlling strain paths — can significantly decrease energy consumption while maintaining forming quality. Although a detailed energy analysis is beyond the scope of the present work, the observed temperature window may thus contribute to more sustainable forming of ZE10A alloy in industrial-scale applications.

4.3. Correlation between XRD results and DRX behavior

The XRD analyses presented in Section 3.2 provide complementary evidence supporting the microstructural observations discussed in Section 4.2. Wide-range diffraction scans confirmed that the ZE10A alloy behaves as a nearly single-phase material in the 250–300 °C interval, with all detectable peaks corresponding to the α-Mg phase ($P6_3/mmc$). The absence of additional reflections related to $Mg_{12}Nd$ or $Mg_{41}Nd_5$ indicates that precipitation is either negligible or below the detectability threshold at these temperatures. However, the local intensity variations of the basal (0002) and {10–12} reflections, particularly the slight reduction in {10–12} twin-related peaks with increasing temperature, reveal subtle structural relaxation processes linked to dynamic recovery and recrystallization. Given that the {10–12} system corresponds to tensile twinning in HCP Mg, the observed attenuation of these reflections indicates the predominance of tensile twins in this temperature/strain window, with no evidence of {10–11} compression or double twins within the detectability/resolution of XRD and OM. Quantitatively, the measured (uncorrected) FWHM of the basal (0002) reflection is 0.164, 0.179, and 0.164° 2θ at 250, 275, and 300 °C, respectively, while (10–10) shows 0.159, 0.179, and 0.167° 2θ (see Table 7). Peak positions remain essentially unchanged (34.420–34.430° 2θ for (0002) and ~32.20–32.21° 2θ for (10–10)). Within the experimental uncertainty and without instrumental-broadening correction, these data do not exhibit a systematic broadening with temperature, supporting the view that residual microstrain and defect density do not increase in this window; rather, the attenuation of {10–12} features is consistent with twin relaxation and limited recovery/incipient DRX.

Our XRD results, combining wide-range scans and focused windows, are consistent with recent findings in Mg alloys. Feng et al. (2023) [52] reported that, in Mg–La–Ce alloys containing Nd, XRD spectra revealed intensified reflections from the $Mg_{12}RE$ phase as Nd content increased, demonstrating that Nd promotes the formation of thermally stable intermetallics which influence high-temperature strength. In contrast, the present ZE10A alloy—nominally a dilute Mg–Nd–Zn–Zr system—did not exhibit such phase development up to 300 °C, confirming that the thermomechanical treatments applied here remain below the threshold for significant precipitation hardening. This behavior reinforces the interpretation that the mechanical response at 250–300 °C is governed primarily by dislocation rearrangement, partial twinning suppression, and incipient DRX rather than by secondary-phase strengthening.

Similarly, Miao et al. (2022) [53] observed, through combined XRD and EBSD analyses, that wide 2θ scans (20–90°) effectively captured the redistribution of basal and non-basal intensities during multi-pass lowered-temperature rolling of AZ31 alloys. Their results demonstrated that progressive DRX reduces internal strain, weakens the basal texture, and enhances the activation of non-basal slips. The trend identified in ZE10A—slight attenuation of {10–12} reflections and stabilization of the basal (0002) peak—is in line with these observations and suggests that temperature-assisted DRX contributes to the relaxation of deformation twins and the gradual transition toward a more equiaxed microstructure, as confirmed by the grain-size results in Section 4.2. Taken together with the attenuation of {10–12} reflections, these trends are indicative of a slight basal texture weakening in ZE10A within the 250–300 °C window. Consistently, no systematic FWHM broadening is detected for (0002) and (10–10) across 250–300 °C (Table 7), indicating that stored microstrain remains low while twinning relaxes and DRX remains limited in magnitude.

Overall, the combination of microstructural and diffraction evidence indicates that, within the studied temperature window, the ZE10A alloy undergoes limited lattice recovery and partial recrystallization while maintaining structural stability. The correlation between the reduction in twin-related XRD intensity and the decrease in the H/V grain-aspect ratio confirms that early stages of DRX take place concurrently with stress relaxation, providing a consistent explanation for the observed balance between strength retention and ductility improvement at

300 °C.

5. Conclusions

Based on the results obtained in this investigation on the ZE10A magnesium alloy, the following conclusions can be drawn:

Increasing the tensile test temperature from 250 °C to 300 °C significantly affected the mechanical properties of the alloy, leading to a progressive reduction in both yield strength (YS) and ultimate tensile strength (UTS). This reduction is associated with the thermal activation of deformation mechanisms, which facilitate dislocation motion and, to a lesser extent, dynamic recrystallization (DRX).

The relatively modest decrease in true strains at UTS (ε_t,UTS) and at fracture (ε_t,f) in this temperature range suggests that the ductility of the alloy was less affected compared to higher temperatures (350–450 °C), where the intensification of DRX leads to a marked improvement in formability. This study did not include quantitative DRX evaluation (e.g., EBSD), which is acknowledged as a limitation and should be addressed in future investigations.

Temperature increase during deformation influenced the microstructure by gradually transforming slightly elongated and twinned grains (predominant at 250 °C) into finer equiaxed grains at 300 °C, due to the onset of DRX. However, grain refinement was limited since the thermal energy was insufficient to trigger large-scale nucleation, and the presence of neodymium (Nd) restricts grain boundary mobility. This was reflected in the small variation of average grain size, from 14.19 μm to 12.61 μm between 250 °C and 300 °C.

Complementary XRD analyses revealed that the ZE10A alloy remains structurally stable within the investigated temperature range. All detectable peaks correspond to the α-Mg phase, and no clear evidence of secondary Mg–Nd compounds (e.g., $Mg_{12}Nd$ or $Mg_{41}Nd_5$) was observed. This behavior is consistent with the nearly single-phase nature of the alloy and the slow precipitation kinetics typical of Nd in ZE-series systems below 350 °C. To substantiate the assessment of residual strain, the FWHM of the (0002) and (10–10) reflections was quantified (measured, uncorrected): (0002) = 0.164, 0.179, 0.164° 2θ and (10–10) = 0.159, 0.179, 0.167° 2θ at 250, 275, and 300 °C, respectively (Table 7). Peak positions remained essentially unchanged, and no systematic FWHM broadening with temperature was detected, supporting low residual microstrain and limited changes in defect density within 250–300 °C.

The observed attenuation of {10–12} twin-related reflections with increasing temperature supports the occurrence of stress relaxation and partial twin annihilation, in agreement with the optical observations. Taken together with the FWHM trends, these diffraction results indicate twin relaxation and early recovery/incipient DRX, and are qualitatively consistent with a slight weakening of the basal texture in this window.

Overall, the findings confirm that DRX in ZE10A within the 250–300 °C range is limited and strongly influenced by Nd, resulting in microstructures with lower grain refinement than those obtained at higher temperatures. The combined XRD and microstructural results demonstrate that this alloy remains structurally stable during low-temperature thermomechanical processing, with lattice integrity maintained and no detectable phase evolution. While this behavior reduces hot formability, it may be advantageous for applications requiring mechanical property retention at elevated temperatures. Moreover, the feasibility of processing the alloy at lower temperatures, even with reduced recrystallization, can contribute to more sustainable manufacturing.

A detailed understanding of this behavior is therefore essential for optimizing thermomechanical processing routes of rare-earth-containing magnesium alloys, balancing microstructural and mechanical requirements with energy efficiency criteria.

Declaration of competing interest

The authors declare that they have no known competing financial interests or personal relationships that could have appeared to influence the work reported in this paper.

Acknowledgements

The authors acknowledge the financial support of the National Council for Scientific and Technological Development (CNPq), the Coordination for the Improvement of Higher Education Personnel (CAPES/PROEX) – Brazil and Bruning Tecnometal.

Appendix A. Supplementary data

Supplementary data to this article can be found online at https://doi.org/10.1016/j.jmrt.2025.10.266.

References

[1] Kulekci MK. Magnesium and its alloys applications in automotive industry. Int J Adv Manuf Technol 2008;39:851–65. https://doi.org/10.1007/s00170-007-1328-5.
[2] Cam G, Gunen A. Challenges and opportunities in the production of magnesium parts by directed energy deposition processes. J Magnesium Alloys 2024;12:1663–86. https://doi.org/10.1016/j.jma.2024.05.004.
[3] Khaliq UA, Yusof F, Chen Z, et al. A comprehensive review on friction stir welding of aluminum with magnesium: a new insight on joining mechanisms by interfacial enhancement. J Mater Res Technol 2023;27:4595–624. https://doi.org/10.1016/j.jmrt.2023.10.158.
[4] Ahmed MMZ, El-Sayed Seleman MM, Fydrych D, Cam G. A review on friction stir welding of dissimilar Al- and Mg-alloys: scientometric analysis and strategies for achieving high-quality joints. J Magnesium Alloys 2023;11:4082–127. https://doi.org/10.1016/j.jma.2023.09.039.
[5] Cam G. Friction stir welded structural materials: beyond Al-alloys. Int Mater Rev 2011;56:1–48. https://doi.org/10.1179/095066010X12777205875750.
[6] Heidarzadeh A, Mironov S, Kaibyshev R, Cam G, Simar A, Gerlich A, Khodabakhshi F, Mostafaei A, Field DP, Robson JD, Deschamps A, Withers PJ. Friction stir welding/processing of metals and alloys: a comprehensive review on microstructural evolution. Prog Mater Sci 2021;117:100752. https://doi.org/10.1016/j.pmatsci.2020.100752.
[7] Blawert C, Hort N, Kainer KU. Automotive applications of magnesium and its alloys. Adv Eng Mater 2004;6:397–408. https://doi.org/10.1002/adem.200300336.
[8] Doege E, Dröder K. Sheet metal forming of magnesium wrought alloys – formability and process technology. J Mater Process Technol 2001;115:14–9. https://doi.org/10.1016/S0924-0136(01)00712-9.
[9] Wu H, Sun P, Lin F. Anisotropic and tensile flow behaviors of Mg alloy AZ31B thin sheet in H24 condition at elevated temperature. Mater Sci Eng, A 2011;528:2522–31. https://doi.org/10.1016/j.msea.2010.11.065.
[10] Jiang N, Liu Y, Guo J, Fan Z, Huang Y. Effect of neodymium, gadolinium addition on microstructure and mechanical properties of AZ80 magnesium alloy. J Rare Earths 2016;34:1075–82. https://doi.org/10.1016/S1002-0721(16)60109-3.
[11] Wei K, Zhang Y, Li C. Grain size effect on tensile properties and slip systems of pure magnesium. Acta Mater 2021;202:237–48. https://doi.org/10.1016/j.actamat.2020.10.062.
[12] Zhang K, Zhou J, Yang Y, Xu L, Chen Y. Evolution of twinning and shear bands in magnesium alloys during rolling at room and cryogenic temperature. Mater Des 2020;192:108731. https://doi.org/10.1016/j.matdes.2020.108731.
[13] Conrad H, Robertson WD. Effect of temperature on the flow stress and strain-hardening coefficient of magnesium single crystals. JOM 1957;9:503–12. https://doi.org/10.1007/BF03399407.
[14] Knezevic M, Levinson A, Harris R, Mishra RK, Doherty RD, Kalidindi SR. Deformation twinning in AZ31: influence on strain hardening and texture evolution. Acta Mater 2010;58:6230–42. https://doi.org/10.1016/j.actamat.2010.07.011.
[15] Ardeljan M, Beyerlein IJ, McWilliams BA, Knezevic M. Strain rate and temperature sensitive multi-level crystal plasticity model for large plastic deformation behavior: application to AZ31 magnesium alloy. Int J Plast 2016;83:90–109. https://doi.org/10.1016/j.ijplas.2016.03.004.
[16] Ardeljan M, Knezevic M, Jain M, Pathak S, Kumar A, Li N, Mara NA, Baldwin JK, Beyerlein IJ. Room temperature deformation mechanisms of Mg/Nb nanolayered composites. J Mater Res 2018;33:1311–32. https://doi.org/10.1557/jmr.2017.471.
[17] Kaseem M, Chung BK, Yang HW, Hamad K, Ko YG. Effect of deformation temperature on microstructure and mechanical properties of AZ31 Mg alloy processed by differential-speed rolling. J Mater Sci Technol 2015;31:498–503. https://doi.org/10.1016/j.jmst.2014.10.004.
[18] Yoshinaga H, Horiuchi R. Deformation mechanisms in magnesium single crystals compressed in the direction parallel to hexagonal axis. Trans 1963;JIM 4:1–8.
[19] del Valle JA, Carreño F, Ruano OA. Influence of texture and grain size on work hardening and ductility in magnesium-based alloys processed by ECAP and rolling. Acta Mater 2006;54:4247–59. https://doi.org/10.1016/j.actamat.2006.05.014.

[20] Luo AA. Applications: aerospace, automotive and other structural applications of magnesium. In: Pekguleryuz MO, Kainer KU, Kaya AA, editors. Fundamentals of magnesium alloy metallurgy. Cambridge: Woodhead Publishing; 2013. p. 266–316.
[21] Yang Y, Xiong X, Chen J, Peng X, Chen D, Pan F. Research advances of magnesium and magnesium alloys worldwide in 2022. J Magnesium Alloys 2023;11:2611–54. https://doi.org/10.1016/j.jma.2023.05.004.
[22] Jafari Nodooshan HR, Wu GH, Liu WC, Wei GL, Li YL, Zhang S. Effect of Gd content on high temperature mechanical properties of Mg-Gd-Y-Zr alloy. Mater Sci Eng, A 2016;651:840–7. https://doi.org/10.1016/j.msea.2016.02.092.
[23] Ali Y, Qiu D, Jiang B, Pan F, Zhang M. Current research progress in grain refinement of cast magnesium alloys: a review article. J Alloys Compd 2015;619: 639–51. https://doi.org/10.1016/j.jallcom.2014.10.161.
[24] Luxfer. Highly formable magnesium sheet. 2018. Luxfer.
[25] ASTM International. ASTM B90/B90M-21: standard specification for magnesium-alloy sheet and plate. West Conshohocken, PA: ASTM International; 2021. https://doi.org/10.1520/B0090_B0090M-21.
[26] Zhang K, Zheng JH, Shao Z, Pruncu C, Turski M, Guerini C, Jiang J. Experimental investigation of the viscoplastic behaviours and microstructure evolutions of AZ31B and Elektron 717 Mg-alloys. Mater Des 2019;184:108182. https://doi.org/10.1016/j.matdes.2019.108182.
[27] Muhammad W, Mohammadi M, Kang J, Mishra RK, Inal K. An elasto-plastic constitutive model for evolving asymmetric/anisotropic hardening behavior of AZ31B and ZEK100 magnesium alloy sheets considering monotonic and reverse loading paths. Int J Plast 2015;70:30–59. https://doi.org/10.1016/j.ijplas.2015.03.004.
[28] Lentz M, Risse M, Schaefer N, Reimers W, Beyerlein IJ. Strength and ductility with double twinning in a magnesium alloy. Nat Commun 2016;7:11068. https://doi.org/10.1038/ncomms11068.
[29] Xu Y, Huang Y, Wang Y, Gan W, Wang S, Maawad E, Schell N, Hort N. Investigations on the tensile deformation of pure Mg and Mg–15Gd alloy by in-situ X-ray synchrotron radiation and visco-plastic self-consistent modeling. J Magnesium Alloys 2023;11:607–13. https://doi.org/10.1016/j.jma.2021.06.011.
[30] Zhu G, Shabalin A, Wang J, Lienert U, Zeng X, Wang L. Effect of strain rate on deformation mechanisms of a Mg alloy. Metall Mater Trans A 2025. https://doi.org/10.1007/s11661-025-07739-y.
[31] Yang B, Vassilev-Galindo V, Llorca J. Application of machine learning to assess the influence of microstructure on twin nucleation in Mg alloys. npj Comput Mater 2024;10:26. https://doi.org/10.1038/s41524-024-01212-x.
[32] Zeng X, Yi S. Deformation mechanisms of magnesium alloys with rare-earth and zinc additions under plane strain compression. Materials 2024;17:33. https://doi.org/10.3390/ma17010033.
[33] Han F, Wang H, Luo X, Hou Z, Wu G, Huang X. Microstructure and texture evolution of hot-rolled Mg-3Gd alloy during recrystallization. Metals 2023;13: 1216. https://doi.org/10.3390/met13071216.
[34] Khan AS, Pandey A, Gnäupel-Herold T, Mishra RK. Mechanical response and texture evolution of AZ31 alloy at large strains for different strain rates and temperatures. Int J Plast 2011;27:688–706. https://doi.org/10.1016/j.ijplas.2010.08.009.
[35] ASTM International. ASTM A370-23: Standard test methods and definitions for mechanical testing of steel products. West Conshohocken, PA: ASTM International; 2023. https://doi.org/10.1520/A0370-23.
[36] ASTM International. ASTM E8/E8M-16ae1: Standard test methods for tension testing of metallic materials. West Conshohocken, PA: ASTM International; 2016. https://doi.org/10.1520/E0008_E0008M-16AE01.
[37] ASTM International. ASTM B557M-15: Standard test methods for tension testing wrought and cast Aluminum- and magnesium-alloy products (Metric). West Conshohocken, PA: ASTM International; 2015. https://doi.org/10.1520/B0557M-15.
[38] ASTM International. ASTM E112-13: Standard test methods for determining average grain size. West Conshohocken, PA: ASTM International; 2013. https://doi.org/10.1520/E0112-13.
[39] ASTM International, ASTM E3-11. Standard guide for preparation of metallographic specimens. West Conshohocken, PA: ASTM International; 2017. https://doi.org/10.1520/E0003-11R17. 2017.
[40] ASM International. ASM handbook, volume 9: metallography and microstructures. Materials Park, OH: ASM International; 2004.
[41] Alrasheedi NH, Ataya S, El-Sayed Seleman MM, Ahmed MMZ. Tensile deformation and fracture of unreinforced AZ91 and reinforced AZ91-C at temperatures up to 300 °C. Materials 2023;16:4785. https://doi.org/10.3390/ma16134785.
[42] Shah SSA, Liu M, Khan A, Ahmad F, Abdullah MR, Zhang X, Xu S, Peng Z. Twinning aspects and their efficient roles in wrought Mg alloys: a comprehensive review. J Magnesium Alloys 2024;12:2201–30. https://doi.org/10.1016/j.jma.2024.02.009.
[43] Beer AG, Barnett MR. Microstructural development during hot working of Mg-3Al-1Zn. Metall Mater Trans A 2007;38:1856–67. https://doi.org/10.1007/s11661-007-9222-5.
[44] Guo Y, Dai Y, Chen P, Zang Q, Zhang Z. Microstructure, hot deformation behavior, and textural evolution of Mg-3Sn-2Al-1Zn-0.6Nd alloy. Metals 2022;12:364. https://doi.org/10.3390/met12030364.
[45] Huang K, Logé RE. A review of dynamic recrystallization phenomena in metallic materials. Mater Des 2016;111:548–74. https://doi.org/10.1016/j.matdes.2016.09.020.
[46] Galiyev A, Kaibyshev R, Gottstein G. Correlation of plastic deformation and dynamic recrystallization in magnesium alloy ZK60. Acta Mater 2001;49: 1199–207. https://doi.org/10.1016/S1359-6454(01)00020-9.
[47] Robson JD. Effect of rare-earth additions on the texture of wrought magnesium alloys: the role of grain boundary segregation. Metall Mater Trans A 2013;45: 3205–12. https://doi.org/10.1007/s11661-013-1773-3.
[48] Jiang MG, Xu C, Nakata T, Yan H, Chen RS, Kamado S. Rare earth texture and improved ductility in a Mg-Zn-Gd alloy after high-speed extrusion. Mater Sci Eng, A 2016;667:233–9. https://doi.org/10.1016/j.msea.2016.04.063.
[49] Hantzsche K, Yi F, Bohlen M, et al. Effect of rare earth additions on microstructure and texture development of magnesium alloy sheets. Scr Mater 2010;63:725–30. https://doi.org/10.1016/j.scriptamat.2010.08.013.
[50] Hadorn JP, Hantzsche K, Yi S, et al. Role of solute in the texture modification during hot deformation of Mg-rare earth alloys. Metall Mater Trans A 2012;43: 1347–62. https://doi.org/10.1007/s11661-011-0923-5.
[51] Gao MD, Wang QY, Li LM, Chen X, Zhang YZ. Energy-economizing optimization of magnesium alloy hot stamping process. Processes 2020;8:186. https://doi.org/10.3390/pr8020186.
[52] Feng L, Dong X, Cai Q, Wang B, Ji S. Effect of Nd on the microstructure and mechanical properties of mg–la–ce alloys at ambient and elevated temperatures. J Mater Eng Perform 2023;32(6):2598–606. https://doi.org/10.1007/s11665-022-06853-x.
[53] Miao Q, Zhu L, Wang W, Wang Z, Shao B, Chen W, Yu Y, Zhang W. Evolution of the microstructure and mechanical properties of AZ31 magnesium alloy sheets during multi-pass lowered-temperature rolling. Metals 2022;12(11):1811. https://doi.org/10.3390/met12111811.